Supporting information for: Swelling and evaporation determine surface morphology of grafted hydrogel thin films

Caroline Kopecz-Muller[1,2,3], Clémence Gaunand[1,2], Yvette Tran[4,5], Matthieu Labousse[1], Elie Raphaël[1], Thomas Salez[3], Finn Box[1,2,6],* and Joshua D. McGraw[1,2]†

[1] *Gulliver, CNRS UMR 7083, ESPCI Paris, Université PSL, 75005 Paris, France*

[2] *Institut Pierre Gilles de Gennes (IPGG), ESPCI Paris, Université PSL, 75005 Paris, France*

[3] *Univ. Bordeaux, CNRS, LOMA, UMR 5798, F-33405 Talence, France*

[4] *Sciences et Ingénierie de la Matière Molle, CNRS UMR 7615, ESPCI Paris, Université PSL, 75005 Paris, France*

[5] *Sorbonne-Universités, UPMC Université Paris 06, SIMM, Université PSL, 75005 Paris, France and*

[6] *Physics of Fluids & Soft Matter, Department of Physics & Astronomy, University of Manchester, Manchester M13 9PL, United Kingdom*

I. EXPERIMENTAL PROTOCOLS

A. Substrate preparation

The hydrogel samples studied here were made on either silicon wafers or thin glass substrates. The chosen substrates are cleaned in a freshly prepared "piranha" solution. 600 mL of this solution is prepared by mixing 200 mL of sulfuric acid (95-97%) and 400 mL of hydrogen peroxide (35%). The resulting solution was left to rest at room temperature for approximately 30 min, until it became a clear solution with no bubbles. The substrates were then immersed in this "piranha" solution for 1 h thoroughly, rinsed with deionized water, dried under pressurized nitrogen flow, rinsed with absolute ethanol, and finally dried again. Freshly cleaned substrates were chemically modified by grafting thiol groups on their surface in order to allow the hydrogel attached to the substrate. 200 mL of silane solution was prepared by mixing 196 mL of absolute ethanol and 4 mL of 3-mercaptopropyltrimethoxysilane; this solution was left to rest for 1 h. Silanization was performed by immersing the substrates in this solution for 1 h. The substrates were then rinsed with absolute ethanol, and dried under nitrogen flow. All substrate preparation steps were done in a clean-room environment.

B. Hydrogel film preparation

The PNIPAM hydrogel used here [1] was prepared from a PNIPAM polymer that has been functionalized with ene-reactive groups, its molar mass is 459 kg/mol. The ene-functionnalized polymer solution was prepared by dissolving the copolymer in a 50/50 mixture of methanol and butanol, at the desired concentration (between 0.5 and 10 wt%). The solution was then left to rest overnight in the fridge. Just before use, dithioerythritol was added as a crosslinker: the quantity added was typically 60 wt% of that of the copolymer dissolved in solution. The solution was left to rest and homogenize for 20 min. The prepared solution was coated on the surface of thiolated substrates by spin-coating, with a spinning time of 30 s and different angular velocities in the range 500 to 4000 rpm (in the case of glass substrates, the solution was filtered with a 0.2 μm calibrated filter prior to spin coating). To remove excess solvent, the resulting polymer films were soft baked at 65°C for 1 min or dried under ambient conditions. Finally, the hydrogel was cross-linked by performing a UV-irradiation (λ_{UV}=254 nm) on the samples, with a fluorescent lamp for 0 min to 3 h (*n.b.* all measurements reported in the main text were performed on samples subject to 3 h of UV-irraditation). To remove uncured polymer and crosslinker excess, the resulting samples were either washed only with isopropanol HPLC grade, or first by immersion in deionized water for 4 h, then in isopropanol HPLC grade for 15 min. Finally, they were dried under ambient conditions.

C. Influence of polymer concentration and spin-coating speed on the film thickness

Sample thickness was modified by changing either the spin-coating speed or the PNIPAM solution concentration in the initial polymer solution (to modify its viscosity). This last parameter has the greatest influence: as shown in Fig. 1, modifying the PNIPAM concentration from 0.5 to 15 wt% allows the film thickness to be varied over almost three orders of magnitude (from $\sim$ 10 nm to 8 μm), for a given angular velocity of spin coating.

D. Influence of UV-exposure time and substrate type on ultrathin samples

Ultrathin samples, with thicknesses smaller than 70 nm, did not show any surface patterning either before or after the rinse step (see main text, Fig. 4). Ad-

* finn.box@manchester.ac.uk

† joshua.mcgraw@espci.fr

ditionally, since the surfaces remained flat, zero dependence on the substrate type or the evaporation rate of the spin-coating solvent was recorded. Ultrathin samples did, however, enable to investigate the influence of UV-exposure time on cross-linking of PNIPAM and the final thickness of the hydrogel films, as we now describe.

Ultrathin hydrogel samples were prepared from a 1% PNIPAM solution, as previously described, spin-coated at 3000 rpm. The samples were subjected to different UV-irradiation times (exposition carried out using a UV lamp, power 8 W, wavelength λ_{UV}=254 nm) and two evaporation methods after spin-coating, that lead to two evaporation rates: soft-baking (2 min at 65°C) or drying under ambient conditions (RT drying). These samples were prepared on two different types of substrate: functionalized silicon wafers and functionalized glass slides. In these particular experiments, samples were only rinsed with isopropanol. They were observed before and after rinse and their thickness was measured, using atomic force microscopy (AFM). When samples were not irradiated with UV (*i.e.* zero insolation time) no hydrogel was observed; the crosslinking network was unable to form, prohibiting the formation of a substrate-attached hydrogel.

Fig. 2 shows the time evolution of the thickness of samples grafted onto silicon wafers that underwent a soft-baking process and were exposed to UV irradiation for different periods of time, before and after rinsing. All the samples studied here were prepared with a 1 wt% PNIPAM solution and were spin-coated at 3000 rpm. We observe that 35 % to 50 % of the sample thickness to be removed during the rinse step. We believe that rinsing removes excess cross-linker and small polymer chains that are not attached to the polymeric network, since the high amount of removed matter is consistent with the proportional excess of cross-linker (nearly 38 wt%). UV-irradiation cures the polymer network – decreasing the amount of free unreacted cross-linker and small unattached chains – accordingly, we see that when UV-exposure time increases, the thickness of the removed portion tends to decrease. Additionally, we observed that the thickness of rinsed samples reaches a plateau at an exposure time of 1h30, suggesting that the cross-linking density would be homogeneous along the depth of the film in the plateau regime.

The results presented in this article were systematically obtained on samples that were exposed to UV for 3h and rinsed. We thus believe that the observed surface patterns do not result from any cross-linking gradient along the thickness of our PNIPAM films, in contrast to the observations of other works [2]. To understand what is the origin of the pattern formation, in the next section we exhibit AFM images of PNIPAM films at different stages of the fabrication process.

II. EMPIRICAL ORIGIN OF PATTERNS

A. Determinant step for the apparition of patterns

Sequential surface examination on dry samples during preparation enables identification of the preparation stage at which patterns appear. In Fig. 3, we show AFM images of two PNIPAM films, at different key steps of the fabrication protocol: right after spin-coating and evaporation of the solvent, after UV insolation, after rinsing in water and drying, and after rinsing in isopropanol and drying. For thinner films (see Fig. 3, first row), no pattern appears. For sufficiently thick samples (see Fig. 3, second row), a surface pattern appears following the first rinsing-and-drying cycle, suggesting that the surface instability results from the swelling-deswelling process of the film. Finally, the subsequent swelling-and-drying cycle does not affect the formed pattern, suggesting that the deformation cycle is irreversible. In summary, the pattern is formed and fixed during the first rinsing-and-drying cycle.

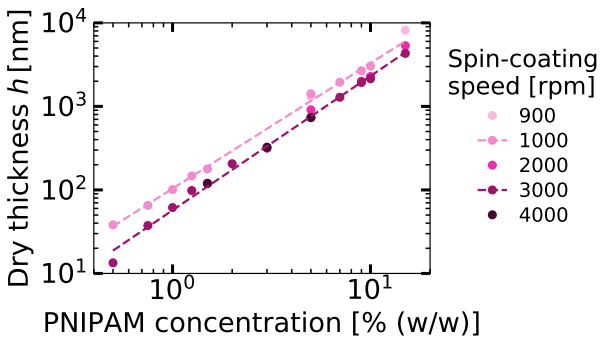

FIG. 1: **Dry thickness of the PNIPAM films as a function of PNIPAM concentration** *Sample thickness in the dry state h after rinsing as a function of PNIPAM solution concentration (wt%), for different spin-coating speeds as indicated by the legend.*

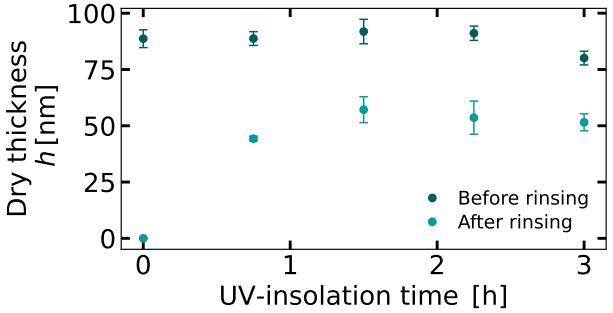

FIG. 2: **Influence of UV-exposure time and rinsing on sample thickness.** *Sample thickness in the dry state h as a function of the UV-insolation time, before and after rinsing. The samples were prepared using a 1 wt% PNIPAM solution and spin-coating velocity of 3000 rpm. The values are averaged on 4 measurements.*

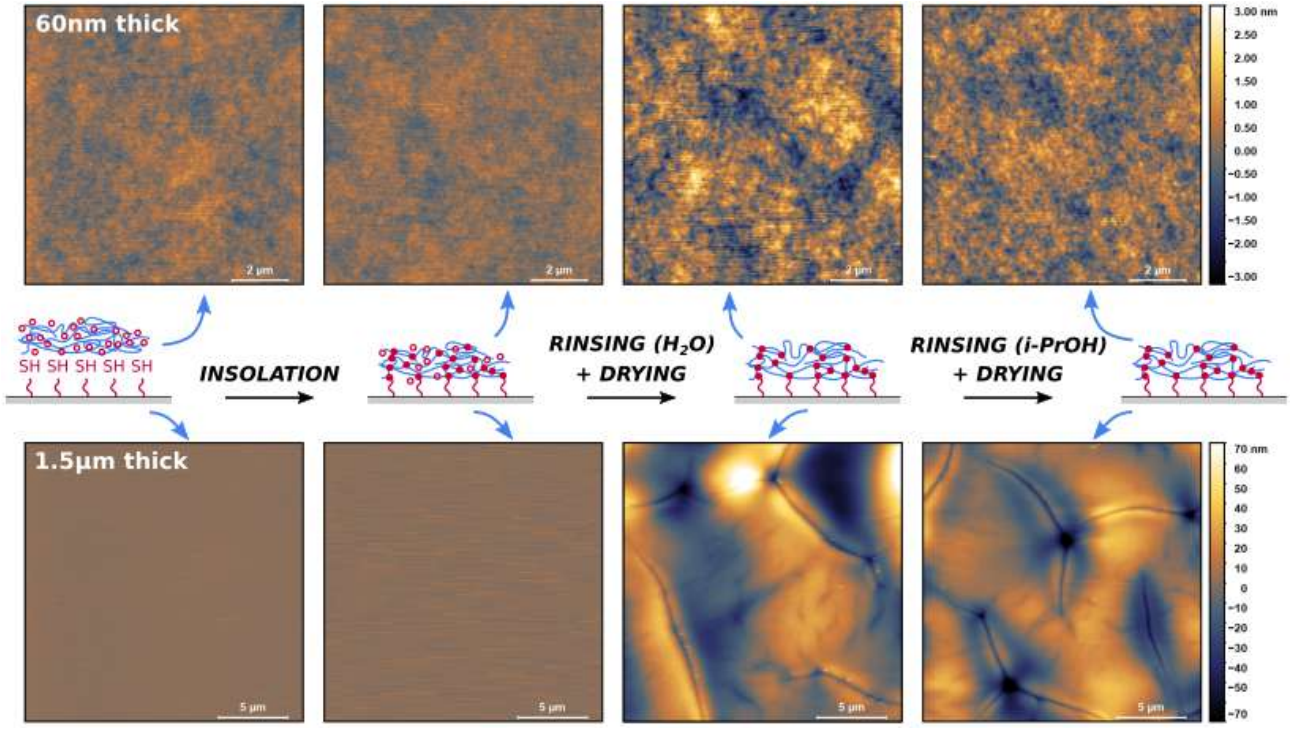

FIG. 3: **Topography of PNIPAM films during the fabrication process.** *AFM images of two dry PNIPAM films, at different steps of the fabrication process : after spin coating, after UV-insolation, after a first rinsing-and-drying cycle in water and after a second one in isopropanol. Top row :* 60 nm *thick sample, fabricated using a spin-coating velocity of 3000 rpm and a PNIPAM solution concentration of 1 wt%. Bottom row :* 1.5 µm *thick sample, fabricated using a spin-coating velocity of 3000 rpm and a PNIPAM solution concentration of 9 wt%.*

B. Influence of the solvent evaporation rate and solvent type on thick samples

The creasing instability appears following immersion and rinsing of the cross-linked hydrogel film in a solvent, as showed in Fig. 3. This confirms that the surface patterning initially appears as a consequence of volumetric change, associated with imbibition-induced swelling, of the grafted, laterally-confined hydrogel. To study the influence of the (re)swelling of hydrogels in successive solvents, fully rinsed hydrogels that exhibited a pattern were immersed in two different, subsequent solvents – water and acetone – after preparation. The samples were then dried under two different conditions; using a nitrogen gun (which encourages a fast evaporation) and under ambient conditions (which results in a slower evaporation). Examples of sequential swelling and drying cycles are shown in Figs 4A and B, while the table shown in Fig. 4C indicates the samples preparation protocols. The surface patterning in a particular region-of-interest was observed on each sample before and after this secondary immersion and drying cycle, and the patterns were compared. For almost all samples, the exact same pattern can be recovered, showing that subsequent immersion and drying cycles had a negligible affect on the initial pattern features; an example is shown in Figs. 4 A and B. For two samples only, a slight amplitude decrease was observed, but is not considered to be a systematic effect of the experiment.

This experiment shows that irrespective of the patterns shape and amplitude, they seem to be fixed and irreversible once they initially formed (*i.e.* during the first swelling and drying process). Our evidence suggests that the evaporation rate and its quality (related to its nature and to what extent it can swell the network) of any subsequent solvents seen by the hydrogel do not influence the surface pattern, contrary to what was evidenced in [3]. Instead, in our experiments, the first solvent seen by the system (*i.e.* water, during the first rinse step) that sets and fixes the pattern, induced network swelling and drying-induced shrinking.

To investigate the influence of evaporation rate of the first solvent on the surface patterning, hydrogels with patterns were prepared and rinsed only in water, with two different evaporation rates: a slow one, allowed by drying under ambient conditions, and a very slow one, achieved by drying in a covered beaker containing a water reservoir, with a small opening in the lid. In the first case, the sample dried in ~ 30 min; in the second case, drying took a few days. As a result, both samples exhibited similar patterns when fully dried. On the basis of this observation, we conclude that, for evaporation on the time scale of minutes to days, the evaporation rate has no influence on the pattern formation at the surface of

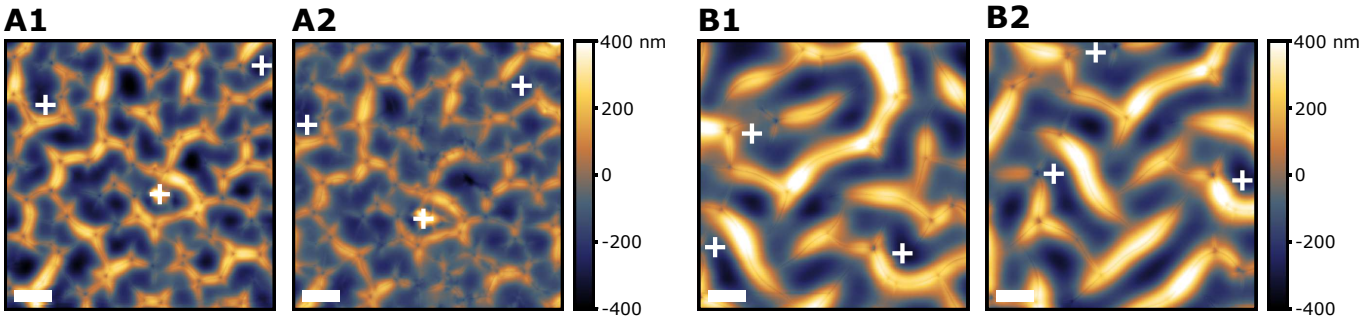

C

Concentration [w/w]	Spin-coating	Solvent	Drying	Result	Images
5%	3000 rpm	Acetone	RT conditions	Exact same pattern	
5%	3000 rpm	Acetone	N_2 drying	Same pattern type	
10%	1000 rpm	Acetone	RT conditions	Exact same pattern	B1 - B2
20%	1000 rpm	Acetone	N_2 drying	Exact same pattern; amplitude decrease	
10%	3000 rpm	Water	RT conditions	Exact same pattern	
10%	3000 rpm	Water	N_2 drying	Exact same pattern; amplitude decrease	A1 - A2
2%	3000 rpm	Water	RT conditions	Same pattern type	
2%	3000 rpm	Water	N_2 drying	Exact same pattern	

FIG. 4: **Comparison of surface topography before and after a swelling/drying cycle in different solvents.** *A) Topography measurement of a dry PNIPAM film, before (A1) and after (A2) immersion into water and drying. B) Same, in acetone. The films were prepared using experimental parameters indicated in panel C. The white bar represents* 15 μm. *The three white crosses are placed on remarkable spots to guide the eye in the comparison. C) Table of immersion experiments and observations. The images showed in panels A and B correspond to two samples, as indicated in the right column.*

our samples.

III. CHARACTERIZATION OF PATTERNS FROM THE AFM IMAGES

A. Distinguishing pattern types and measuring the wavelength

Once the PNIPAM films were imaged by AFM, several tools were used to rationalize the distinction between brain-like and volcano patterns, and measure a wavelength and an amplitude.

Height profiles: From an AFM measurement of the surface topography, the height profile along a line is extracted as showed in Figs. 5A and B, then a wavelength λ and an amplitude A are computed. For a given image, between 10 and 20 profiles are extracted, and measurements of wavelength and amplitude are averaged. The resulting error on the measured wavelength and amplitude, respectively, is about 5 % and 15 % or less. This manual method efficiently permits us to distinguish between the pattern types, as the height profiles exhibit different features in the cases of brain-like and volcano patterns. Indeed, the height profile extracted from images of samples exhibiting a brain-like pattern (Fig. 5A) shows typical creases with sharp and discontinuous slopes, while the height profile extracted from images of samples exhibiting a volcano pattern (Fig. 5B) appears generally sinu-

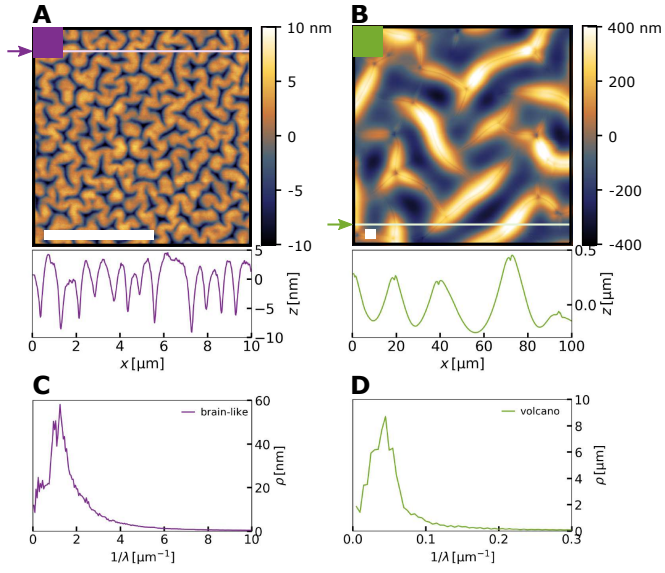

FIG. 5: **Examples of height profiles anf Fourier spectra obtained on typical brain-like (left) and volcano (right) pattern images**. *A) and B) Typical AFM images and height profile extracted along the indicated line. The white bar represents* 5 μm. *C) and D) radial averages of 2D Fourier transforms of images showed respectively in panels A) and B) The obtained spectra are showed as a function of the wavenumber* $1/\lambda$.

soidal, with smooth valleys and reminiscences of sharp creases on the crests.

Fourier transform: From the AFM image of a patterned surface, we compute the 2D Fourier transform and perform a radial average of the 2D spectra. In particular, we show in Figs. 5C and D the averaged spectra obtained from the typical brain-like and volcano patterns showed in Figs. 5A and B. The density ρ is plotted as a function of the wavenumber $1/\lambda$. The wavenumber for which the density reaches a maximum gives a measurement of the dominant wavelength.

The wavelength measurement obtained with the Fourier-based method is consistent with the one obtained with the manual method previously described, however the Fourier-based method is less precise. Indeed, a typical image showing patterns with a good resolution usually shows between 5 and 20 spatial periods, which is not enough to precisely compute the Fourier transform.

Minkowski functionals: From the 3D AFM measurements of the surface topography we compute Minkowski functionals [4, 5]. In particular, the Minkowski area $\mathcal{A}_{\mathrm{Mink}}$, perimeter $\mathcal{P}_{\mathrm{Mink}}$, and connectivity χ_{Mink} were measured as a function of height z (and correspond to the area enclosed by an isocontour, the total length of the isocontours, and number of connected components in an isocontour). Minkowski functionals provide a method of distinguishing 3D patterns with different morphologies [6] since morphologically-equivalent patterns exhibit the same functional dependence on surface height.

In figure 6, we show the Minkowski functionals computed from the AFM images showed in Fig. 5A and B. The Minkowski functionals clearly demonstrate that the two morphologies are geometrically distinct from one another. For our purposes, the skewness of χ_{Mink} as a function of z/A, as showed in Fig. 6C, serves to aid classification of patterns as either brain-like or volcano-like.

In summary, the distinction between pattern types was based on the height profiles, and checked by plotting the Minkowski functionals or simply the height distribution. The measurement of the wavelength and amplitude was also on the height profiles analysis too.

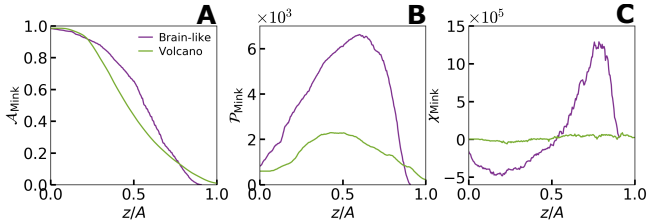

FIG. 6: **Minkowski functionals of brain-like and volcano patterns** *Minkowski functionals, calculated from the images showed in Figs. 5A and B. A) Minkowski area $\mathcal{A}_{\mathrm{Mink}}$, B) perimeter $\mathcal{P}_{\mathrm{Mink}}$, and C) connectivity χ_{Mink} measured as a function of height z, normalized by the amplitude of surface topography A.*

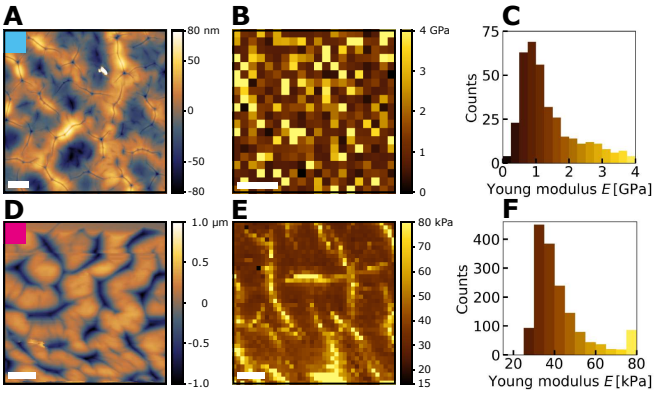

FIG. 7: **Measurement of the Young's modulus of PNIPAM films** *A) AFM image of the investigated region, in the dry state. The white bar represents 5 μm. B) Measured Young's modulus E as a function of the position of the measurement. C) Histogram of the measured values of Young's modulus. D,E and F) same as A, B and C respectively, in the swollen state. The PNIPAM film used here was fabricated using a polymer solution concentration of 5 wt% and a spin-coating velocity of 2500 rpm.*

B. Dry and wet PNIPAM film stiffnesses

Force spectroscopy measurements were performed using AFM on both dried and wet films to extract their Young's modulus, as represented in Fig. 7. Prior to the spectroscopy measurement, the deflection sensitivity was calibrated for each probe on a hard surface, and the spring constant was measured from thermal noise [7]. The AFM measurements on dry and wet films were performed respectively using a sharp and standard tip (*Nanosurf*, model *Dyn190Al*, nominal stiffness 48 N/m) in tapping mode, and using a thin cone-shaped tip (*Nanosensors*, model *qp-BioAC-Cl*, nominal stiffness 0.06 N/m). The indentation range was kept small compared to the sample thickness and the drive approach velocity was slow to minimize the influence of Stokes drag. The AFM data were treated using the *AtomicJ* software [8], based on JKR model, taking into account the probe geometry and the finite thickness of the samples. In Figs. 7A and B we show respectively a typical AFM image of a patterned dried PNIPAM film and the measured Young's modulus as a function of the position of the measurement. On Fig. 7C, we show an histogram of the measured values of Young's modulus, we finally retain $E^{\mathrm{dry}} \approx 700 \pm 100$ MPa as the Young's modulus of dried PNIPAM films. In Fig. 7D we show an AFM image of the same sample as in Fig. 7A but in the swollen state, which exhibit a creased pattern. In fig. 7E we show the measurement of the Young's modulus as a function of the position. Interestingly, the pattern shown on the AFM image can be guessed on the Young's modulus map. Un-

like for dried films, we observe that the Young's modulus varies with the topography: the swollen gel is softer on the top of the bumps than in the depth of the dips. The latter observation may be due to an inhomogeneity of solvent fraction at the surface due to the crease-induced expulsion of solvent, and is consistent with a higher strain close to the creases [9]. Lastly, in Fig. 7F we show the histogram of the measured values of Young's modulus. We finally retain $E^{\mathrm{wet}} \approx 35 \pm 5\,\mathrm{MPa}$ as the Young's modulus of swollen PNIPAM gels. We verified that the measured Young's modulus is independent on the pattern, having checked also on brain-like and volcano samples.

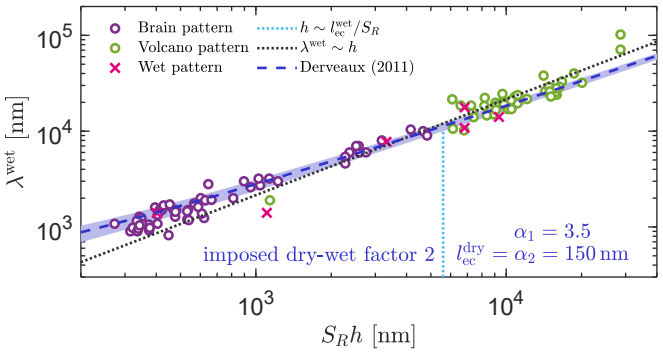

FIG. 8: **Estimation of the dry elastocapillary length** *Wavelength in the wet state λ^{wet} as a function of the wet thickness $S_R h$, using the period-doubling hypothesis as formulated in Eq.* (1). *The dark blue dashed line represents the fitted curve based on Eq.* (2) *[10]. The shaded zone account for a* $\pm 50\,\%$ *of the fitting parameter α_2, that gives an estimate of the dry elastocapillary length.*

C. Precision of the estimation of the dry elastocapillary length

Based on observations, the wavelength of surface patterns in the swollen state λ^{wet} is expected to follow a period-doubling hypothesis:

$$\lambda^{\mathrm{wet}} = \begin{cases} 2\lambda & \text{for} \quad h \leq l_{\mathrm{ec}}^{\mathrm{wet}}/S_R, \\ \lambda & \text{for} \quad h \geq l_{\mathrm{ec}}^{\mathrm{wet}}/S_R, \end{cases} \tag{1}$$

with λ the wavelength in the dry state, and $l_{\mathrm{ec}}^{\mathrm{wet}}/S_R$ the observed thickness transition between brain–like and volcano patterns. With this assumption, the wavelength in the wet state as a function of the thickness is fitted with Dervaux and Ben Amar's model, as:

$$\lambda^{\mathrm{wet}} = \alpha_1 4\pi h / \ln(44.953 h/\alpha_2), \tag{2}$$

with α_1 and α_2 being two fitting parameters, as represented on Fig. 8. In particular, α_2 gives a lengthscale, that estimates the elastocapillary length computed in the initial dry state, $l_{\mathrm{ec}}^{\mathrm{dry}}$. We obtain a prefactor of $\alpha_1 = 3.46$ and a dry elastocapillary length of $l_{\mathrm{ec}}^{\mathrm{dry}} \approx \alpha_2 = 150\,\mathrm{nm}$. To indicate the precision of the estimated lengthscale in the dry state, the shaded area in Fig. 8 indicates how the fitted curve would be affected by a change in the interval $l_{\mathrm{ec}}^{\mathrm{dry}} \pm 50\,\%$. Indeed, the non-linear fit on Dervaux and Ben Amar's model does not provide a precise value, but an estimate for the dry elastocapillary length, and thus for a dry shear modulus of $G^{\mathrm{dry}} \approx 280\,\mathrm{kPa}$. The latter shear modulus would correspond the one of the dry polymer films and would seem perfectly reasonable for a dry polymer film, if the PNIPAM did not undergo a glass transition upon drying. However, the estimate of $l_{\mathrm{ec}}^{\mathrm{dry}}$ is reasonable enough to validate the use of Dervaux and Ben Amar's thickness-wavelength relation to explain our experimental data. As a conclusion, creases are formed at the free surface in the wet state with a prescribed spacing, which scales with the thickness albeit a logarithmic correction.

[1] M. Li, B. Bresson, F. Cousin, C. Frétigny, and Y. Tran, Submicrometric films of surface-attached polymer network with temperature-responsive properties, Langmuir **31**, 11516–11524 (2015).

[2] D. Chandra and A. Crosby, Self-wrinkling of uv-cured polymer films, Adv. Mater. **23**, 3441 (2011).

[3] O. Ortiz, A. Vidyasagar, J. Wang, and R. Toomey, Surface instabilities in ultrathin, cross-linked poly(n-isopropylacrylamide) coatings, Langmuir **26**, 17489–17494 (2010).

[4] K. R. Mecke, Integral geometry in statistical physics, Int. J. Modern Phys. B **12**, 861 (1998).

[5] R. Fetzer, M. Rauscher, R. Seemann, K. Jacobs, and K. Mecke, Thermal noise influences fluid flow in thin films during spinodal dewetting, Phys. Rev. Lett. **99**, 114503 (2007).

[6] C. Scholz, G. E. Schröder-Turk, and K. Mecke, Pattern-fluid interpretation of chemical turbulence, Phys. Rev. E. **91**, 042907 (2015).

[7] H.-J. Butt, B. Cappella, and M. Kappl, Force measurements with the atomic force microscope: Technique, interpretation and applications, Surf. Sci. Rep. **59**, 1 (2005).

[8] P. Hermanowicz, M. Sarna, K. Burda, and H. Gabryś, Atomicj: an open source software for analysis of force curves, Rev. Sci. Instrum. **85** (2014).

[9] S. Karpitschka, J. Eggers, A. Pandey, and J. H. Snoeijer, Cusp-shaped elastic creases and furrows, Phys. Rev. Lett. **119**, 198001 (2017).

[10] J. Dervaux and M. Ben Amar, Buckling condensation in constrained growth, J. Mech. Phys. Solids **59**, 538 (2011).